This is a “preproof” accepted article for *Mineralogical Magazine*.

This version may be subject to change during the production process.

10.1180/mgm.2024.105

Zirconolite $CaZrTi_2O_7$ from the Kovdor phoscorites and carbonatites (Kola Alkaline Province): composition, recrystallization and thermal expansion

Ruiqi Chen[1,2], Anatoly N. Zaitsev[3,4], Oleg I. Siidra[1,5*], John Spratt[6], Alla V. Dolgopolova[4]

[1]Department of Crystallography, St. Petersburg State University, University Embankment, 7/9, St. Petersburg, 119034, Russia

[2]Univ. Lille, CNRS, Centrale Lille, Univ. Artois, UMR 8181, UCCS, Unité de CatalyseetChimie du Solide, F-59000 Lille, France

[3]Department of Mineralogy, St. Petersburg State University, University Embankment, 7/9, St. Petersburg, 119034, Russia

[4]The Centre for Russian and Central EurAsian Mineral Studies (CERCAMS), The Natural History Museum, Cromwell Road, London SW7 5BD, UK

[5]Kola Science Center, Russian Academy of Sciences, Apatity, Murmansk Region, 184200 Russia, 683006, Russia

[6]Imaging and Analysis Centre, The Natural History Museum, Cromwell Road, London SW7 5BD, UK

*o.siidra@spbu.ru

Abstract

This study investigates geologically old, ca. 370 Ma, metamict zirconolite from the Kovdor phoscorites and carbonatites (Kola Alkaline Province). Mineral composition, crystallization behavior, and thermal expansion of the recrystallized samples were analyzed using electron microprobe analysis, Raman spectroscopy, and *in-situ* high-temperature powder X-ray diffraction (HTPXRD). Studied zirconolite crystals are different in their morphology, internal texture, composition, alteration degree, and divided into four distinct groups. The zirconolite is a high Nb and Fe^{3+} variety (10.8-24.1 wt% Nb_2O_5 and 7.9-9.0 wt% Fe_2O_3), it is enriched in Th (up to 8.7 wt% ThO_2), Ta (up to 5.3 wt% Ta_2O_5) and rare earth elements (up to 5.0 wt% REE_2O_3). Raman spectroscopy confirmed that metamict zirconolite is anhydrous.

The recrystallization process of the metamict zirconolite is complex, as detected by HTPXRD. A fluorite-type phase starts to crystallize at 420 °C. The formation of a pyrochlore phase can be identified at 750 °C. The major phases detected in the sample after the recrystallization are: zirconolite-3*T* (53 wt%), srilankite (25 wt%), pyrochlore (15 wt%), baddeleyite (5 wt%) and zircon (3 wt%). The average coefficients of thermal expansion (CTE) values in the temperature range 25-1200 °C are as follows: $\overline{\alpha_a} = \overline{\alpha_b} = \overline{\alpha_{11}} = \overline{\alpha_{22}} = 8.95 \cdot 10^{-6} °C^{-1}$. Similarly, the thermal expansion along the *c*-axis yields a similar value: $\overline{\alpha_a} = \overline{\alpha_b} = 8.93 \cdot 10^{-6}$ °C^{-1}, indicating an almost isotropic thermal expansion of zirconolite-3*T*. The lower CTE value compared to a pure synthetic zirconolite observed in our study for zirconolite-3*T* may be attributed to the complex chemistry and polyphase nature of the studied material.

Keywords: zirconolite; Kovdor; metamict minerals; recrystallization; thermal expansion.

Introduction

Zirconolite, ideally $CaZrTi_2O_7$, was first described by Borodin *et al.* (1956), see also Bulakh *et al.* (2006), from the calcite-amphibole-clinopyroxene rock occurring in central part of the Afrikanda alkali-ultramafic complex, Kola Alkaline Province (Kukharenko *et al.*, 1965; Chakhmouradian and Zaitsev, 1999, 2002, 2004; Zaitsev and Chakhmouradian, 2002). Subsequently, at Kola, the mineral was found in phoscorites and carbonatites from Kovdor, Vuoriyarvi, Seblyavr and TuriyMys (Chakhmouradian and Williams, 2004, and references herein). Zirconolite occurrences, however, are not restricted to phoscorite/carbonatite complexes only. The mineral is known from a wide range of silicate rocks, and even skarns (e.g., Williams and Gieré, 1996, and references herein, Pascal *et al.*, 2009, Zubkova *et al.*, 2018).

Compositionally, zirconolite is characterized by complex element substitution, and may contain significant amounts of Nb, Fe, rare earth elements (REE), U and Th (e.g., Williams and Gieré, 1996; Gieré*et al.*, 1998; Bellatreccia *et al.*, 1999, 2002; Della Ventura *et al.*, 2000; Pascal *et al.*, 2009; Sharygin *et al.*, 2016). The presence of U and Th in zirconolite, especially in geologically old rocks, leads to the damage of crystal

https://doi.org/10.1180/mgm.2024.105 Published online by Cambridge University Press

structure and mineral metamictization. Young zirconolite, however, exhibits crystalline characteristics, even in Th and U-rich varieties, making it suitable for single crystal X-ray analysis (e.g., Zubkova *et al.*, 2018). Besides zirconolite importance as a host for high-field-strength and rare earth elements (Chakhmouradian and Williams, 2004), and mineral-geochronometer (Wu *et al.*, 2010), synthetic zirconolite has been considered as a major component for SYNROC materials (e.g., Lutze and Ewing, 1988).

Zirconolite, both natural and synthetic, fulfills the various requirements for a titanate ceramic matrix for high-level waste (HLW), such as the ability to include a wide range of elements, radiation tolerance, and mechanical durability (Kessoft*et al.*, 1983; Zhang *et al.*, 2018; Yudintsev *et al.*, 2022). This makes it an essential component for such applications (Kessoft *et al.*, 1983; Zhang *et al.*, 2018). The structure of the zirconolite framework is typically characterized as being split into layers consisting of two distinct topologies. Depending on the composition and formation conditions, zirconolite may form the following polytypes: 2*M*, 3*O*, 3*T*, and 4*M* (Cheary and Coelho, 1997; Coelho *et al.*, 1997; Vance *et al.*, 2002; Gilbert *et al.*, 2010; Whittle *et al.*, 2012). Although numerous studies have been conducted to examine the impact of cation doping on polytype crystallization (Coelho *et al.*, 1997; Vance *et al.*, 2002; Gilbert *et al.*, 2010; Ji *et al.*, 2021), the effect of polytype performance on HLW immobilization has not been thoroughly investigated. Various polytypes of crystalline zirconolite mineral samples have been studied, including 2*M* (Chukanov *et al.*, 2014), 3*O* (Zubkova *et al.*, 2018; Chukanov*et al.*, 2019), and 3*T* (Zubkova *et al.*, 2018). The intricate chemistry of natural minerals and the insights gained from polytype crystallization provide valuable insights into predicting the preferred polytype that may emerge from the metamict zirconolite in SYNROC in response to temperature rise.

Herein we present a thorough investigation of geologically old, ca. 370 Ma, metamict zirconolite from the Kovdor phoscorites and carbonatites (Kola Alkaline Province), encompassing thermal annealing experiments, crystallization behavior, and thermal expansion of the (re)crystallized sample.

Zirconolite at Kovdor

The Kovdor complex (~42 km^2) belongs to the Devonian Kola Alkaline Province (Figure 1; Kukharenko et al., 1965; Amelin and Zaitsev, 2002; Krasnova et al., 2004; Downes et al., 2005; Zaitsev et al., 2015; Ivanyuk et al., 2016). Phoscorite and carbonatites form a vertical body, ~1×1.5 km, in the southwestern part of the Kovdor intrusion. Field relations, modal mineralogy and whole-rock compositions suggest that phoscorites are represented by at least ten varieties (with highly variable content of forsterite, apatite, magnetite, phlogopite, tetraferriphlogopite, calcite and dolomite). Carbonatites are calcite, calcite-dolomite and dolomite. Calcite carbonatites, however, are different in minor and accessory minerals, and two varieties are distinguished: calcite carbonatite with phlogopite and calcite carbonatite with tetraferriphlogopite.

https://doi.org/10.1180/mgm.2024.105 Published online by Cambridge University Press

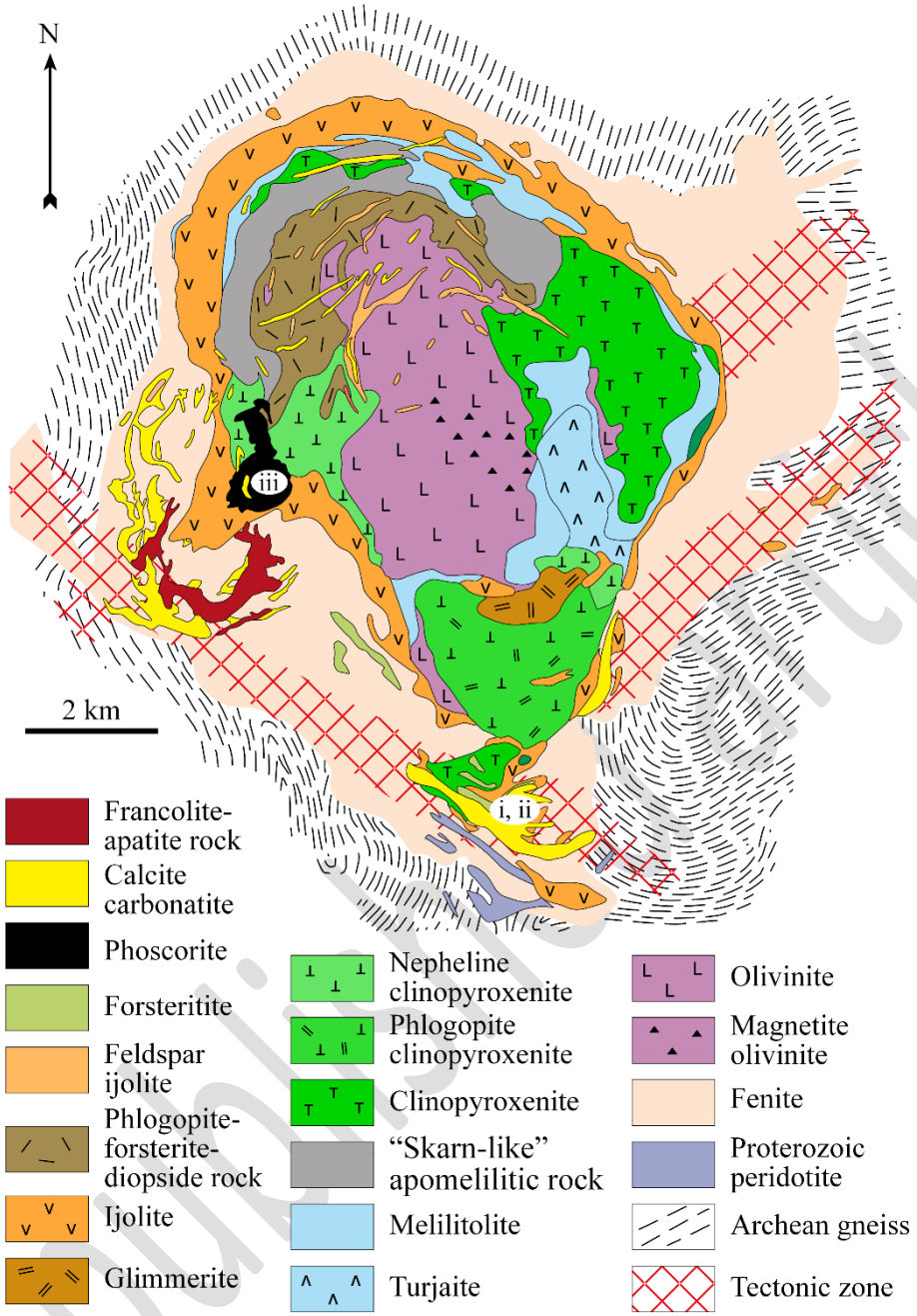

Figure 1. Geological map of the Kovdor utrabasic-alkaline rocks-phoscorite-carbonatite complex (Krasnova et al., 2004, Fig. 4.1). i, ii and iii – locations of the studied zirconolite samples. Published with permission from Cambridge University Press.

Both phoscorite and carbonatites contain diverse Zr and Nb minerals; these include baddeleyite, pyrochloge-group minerals, zirconolite and rare calzirtite, lueshite and isolueshite (Rimskaya-Korsakova, 1963; Kukharenko *et al.*, 1965; Kirillov and Burova, 1967; Kapustin, 1980; Strelnikova and Polezhaeva, 1981; Williams, 1996; Subbotin and Subbotina, 2000; Ivanyuk *et al.*, 2002; Chakhmouradian and Williams, 2004; Zaitsev *et al.*, 2015, 2017). Zirconolite, originally described as zirkelite by Kukharenko et al. (1965), occurs in several varieties of phoscorites and carbonatites, such as: (i) calcite-forsterite-magnetite phoscorite with phlogopite, (ii) calcite carbonatite with forsterite and phlogopite, (iii) calcite-forsterite-magnetite phoscorite

https://doi.org/10.1180/mgm.2024.105 Published online by Cambridge University Press

with tetraferriphlogopite, and (iv) calcite carbonatite with tetraferriphlogopite (Williams, 1996; Zaitsev *et al.*, 2015). The mineral is extremely rare in phoscorites and carbonatites containing phlogopite, but relatively abundant in phoscorites and carbonatites with tetraferriplogopite.

Three compositional varieties of zirconolite are recognized by Zaitsev *et al.* (2015) as follows: (i) REE- and Nb-rich zirconolite (9.5–17.8 wt.% REE_2O_3 and 18.4–22.8 wt.% Nb_2O_5) in calcite–forsterite–magnetite phoscorite with phlogopite, (ii) REE- and Nb-poor zirconolite (<0.05 wt.% REE_2O_3 and 3.7 wt.% Nb_2O_5) in calcite carbonatite with forsterite and phlogopite, and (iii) REE-enriched and Nb-rich zirconolite (2.5–6.3 wt. REE_2O_3 and 15.8–22.2 wt.% Nb_2O_5) in phoscorite and carbonatite containing tetraferriphlogopite. REE-rich zirconolite probably contains elevated amount of nöggerathite end-member, and Nb-rich zirconolite could be enriched in stefanweissite end-member (Chukanov et al., 2018, 2019).

Zirconolite, as zirkelite, was also described from carbonatites that occur in the southern part of the complex and hosted by ijolites and fenites (Osokin, 1979). Carbonatites are calcite and dolomite-calcite. The former are divided in three distinct varieties with minor to major silicates such as (i) aegirine-diopside±orthoclase and Ti-bearing andradite ("melanite"), (ii) phlogopite±diopside, and (iii) forsterite. Zirconolite in calcite carbonatites occurs as tabular (platy) crystals with triangular, cubic or cuboctahedron crystals. Compositionally, zirconolite from the southern calcite carbonatites is similar to that hosted within tetraferriphlogipte-bearing phoscorites and carbonatites (2.5-5.2 wt% REE_2O_3 and 14.0-33.4 wt% Nb_2O_5); however, both cubic and cuboctahedron zirconolite contain a significant amount of Na (1.6-2.4 wt% Na_2O) (Osokin, 1979). Since bulk samples were analyzed by wet chemical analysis, the presence of Na and high Nb content suggests a significant amount of other mineral(s) in the analyzed zirconolite samples.

Samples and Methods

In this study we have used material from collections of heavy mineral fractions (collected by O.M. Rimskaya-Korsakova, N.I. Krasnova and A.N. Zaitsev) from southern carbonatites and phoscorites-carbonatites from the southwestern part of Kovdor (Figure 1). The studied samples are (i) euhedral tabular crystals (southern carbonatites), (ii) euhedral cubic crystals (southern carbonatites), and (iii) euhedral to subhedral prismatic crystals, fragments of broken crystals and unhedral crystals (southwestern phoscorite-carbonatites with tetraferriphlogopite).

Metamict zirconolite crystals, mounted in blocks, were studied by scanning electron microscopy (SEM), using a JEOL 5900LV SEM, with an Oxford instruments Energy Dispersive X-ray Spectrometer (EDS) at the Natural History Museum (London). Zirconolite has been analyzed using a Cameca SX-100 electron microprobe, with wavelength dispersive X-ray spectrometers (WDS) (NHM, London, Tables 1 and 2). 138 spot analyses

https://doi.org/10.1180/mgm.2024.105 Published online by Cambridge University Press

were acquired under the following analytical conditions: 20 kV accelerating voltage, 20 nA beam current and 1 μm beam diameter. Probe standards used were well-characterized natural minerals and synthetic compounds.

All heated crystals were studied using a Hitachi S-3400N (SEM), equipped with an Oxford Instruments X-Max 20 (EDS), (St. Petersburg State University, Table 3). Quantitative analyses were performed with an accelerating voltage of 20 kV and a beam current of 1.8 nA. Acquisition time was 30 s, with a resolution up to 4 nm. The following standards were used for the quantification: MAC (Micro Analysis Consultants Ltd., United Kingdom) and Geller reference standards (Geller microanalytical laboratory).

Raman spectra were acquired by the means of a Horiba Jobin-YvonLabRamHR800 Raman spectrometer (St. Petersburg State University), equipped with Olympus BX41 optical microscope with a resolution of 2 cm^{-1} and the laser beam spot size of 5 μm. Raman spectra were excited by the means of both 532 nm laser. The data processing was performed using CrystalSleuth software.

The recrystallization of zirconolite was studied in air by high-temperature powder X-ray diffraction (HTPXRD) using a Rigaku Ultima IV diffractometer (CoKα radiation, 40 kV/30 mA, Bragg–Brentano geometry, PSD D-Tex Ultra, St. Petersburg State University) with a thermo-attachment in the range 30–1200 °C with the step of 30 °C. A finely ground sample was deposited on a platinum sample holder (20 × 12 × 1.5 mm^3) from an ethanol suspension. Phase analysis was performed using PDF-2 database (2020), PDXL (Rigaku, 2016) and TOPAS V.5.0 (Bruker, 2011) software.

The thermal expansion of zirconolite was studied using the same equipment and conditions. The visualization and calculation of the thermal expansion was performed using the RTT program package (Bubnova *et al.*, 2018).

All studied zirconolite crystals are metamict and in the text below we refer to them as MZ (metamict zirconolite), and recrystallized zirconolite obtained by heating of metamict samples as RZ (recrystallized zirconolite).

Internal zoning and composition of metamict zirconolite

The studied zirconolite crystals are classified into four groups based on their morphology and internal zoning. The MZ-A group is represented by euhedral tabular (platy) crystals from southern carbonatites. They are similar morphologically, to some of the zirkelite crystals from Seblyavr phoscorites and carbonatites described by Bulakh et al. (1998). Backscattered electron images (BSE), show that all crystals are characterized by well-developed zoning with a brighter core and darker rim (Figure 2a). Crystal rims always show a rhythmic-type zonation with concentric strips that are parallel to the crystal edges. One of the studied zirconolite crystals is characterized by well-developed sector- and rhythmic-type zoning (MZ-A^A, Figure 2b).

The second group, denoted as MZ-B, is represented by euhedral cubic zirconolite crystals also occurring in southern carbonatites. The BSE images of all studied crystals show that they consist of the intergrowths of two minerals, pyrochlore and zirconolite (Figure 2c). This can be explained through the structural relationship between zirconolite and pyrochlore (Coelho *et al.*, 1997; Grey *et al.*, 2003). Observed intergrowths of

https://doi.org/10.1180/mgm.2024.105 Published online by Cambridge University Press

zirconolite and pyrochlore explain high sodium content in cubic zirconolite crystals analyzed by Osokin (1979). The presence of Na in zirconolite from Kovdor phoscorite (0.7 wt% Na_2O) was also reported by Kukharenko *et al.* (1965).

MZ-C and MZ-D zirconolite groups are from phoscorites and carbonatites containing tetraferriphlogopite from the southwestern part of the complex. MZ-C is zirconolite occurring in association with pyrochlore and rarely baddeleyite (Figure 2d; see also Fig. 1a in Williams, 1996, and Fig. 8 in Zaitsev *et al.*, 2015). It occurs as euhedral to subhedral prismatic crystals, and BSE images often show heterogeneous internal structure and composition. The compositional disparities may be attributed to distinct zones of crystal growth (sector-type zoning, as depicted in Figure 2d), and certain crystals exhibit late-stage mineral alteration.

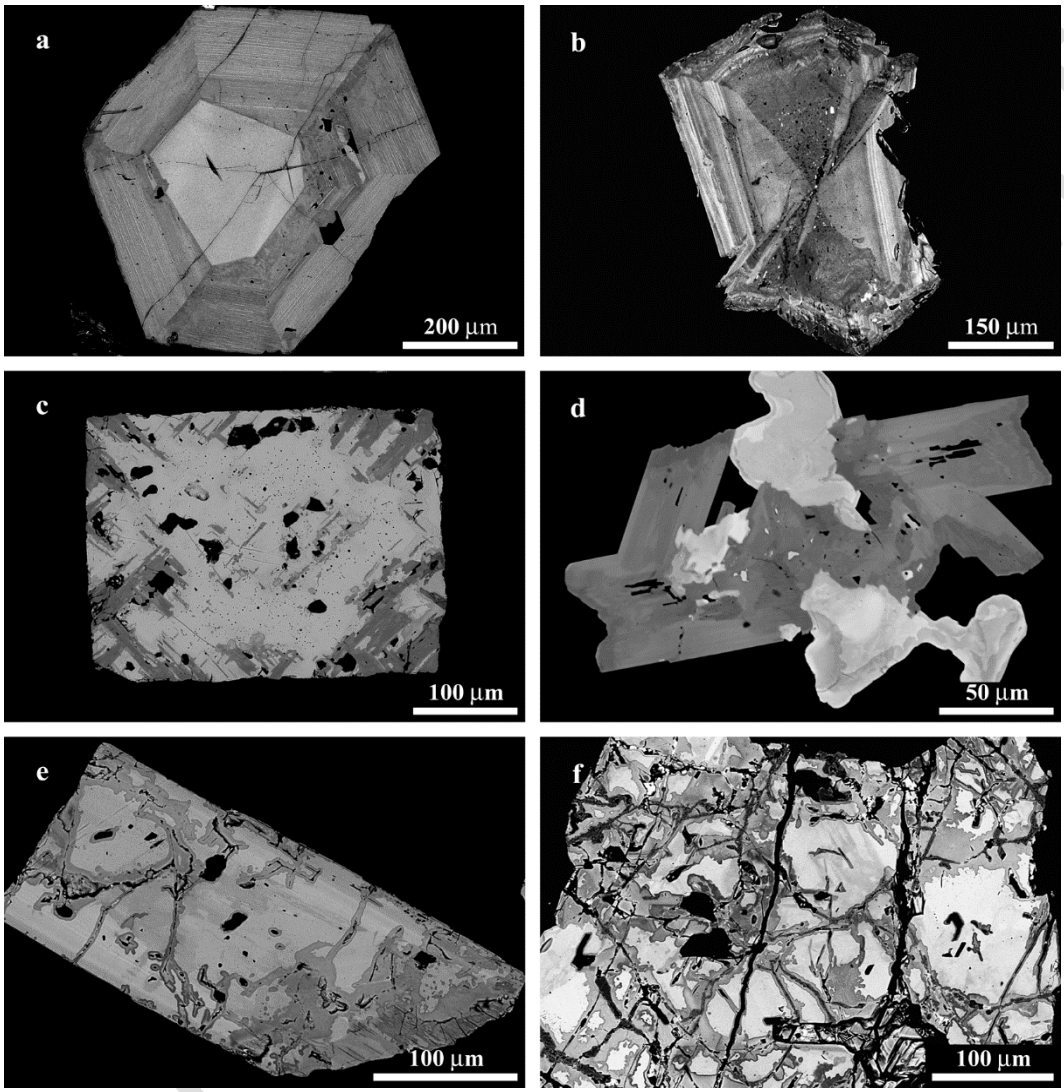

Figure 2. Morphology and internal texture of studied zirconolite: (a) euhedral tabular crystal with rhythmic-type zoning (MZ-A group), (b) euhedral crystal with rhythmic- and sector- type zoning (MZ-A^A group), (c) cubic crystal with pyrochlore (grey) and zirconolite (dark grey) (MZ-B group), (d) zirconolite (dark grey)-pyrochlore(light grey and white) intergrowth (MZ-C group), (e) euhedral crystal showing variable degree of mineral alteration (dark grey areas) (MZ-D group), and (f) internal texture of highly altered (grey and dark grey) subhedral crystal. Back-scattered electron images.

https://doi.org/10.1180/mgm.2024.105 Published online by Cambridge University Press

MZ-D zirconolite occurs as euhedral to subhedral prismatic crystals and fragments of broken crystals. All studied crystals in this group exhibit microcracks and BSE images suggest significant alteration in the mineral composition (Figure 2e, f). Similar alteration textures were previously observed for zirconolite from Afrikanda (Bulakh *et al.*, 2006).

Selected zirconolite composition and calculated atoms per formula units (apfu) values are presented in Table 1.

Limited published data for Kovdor zirconolite (wet chemistry method in Kukharenko *et al.*, 1965 and Osokin, 1979, and electron probe microanalysis in Williams, 1996 and Zaitsev *et al.*, 2015) show highly variable compositions. Our new data confirm previous zirconolite composition variability. The studied zirconolite is strongly enriched in Nb (10.8-24.1 wt% Nb_2O_5), contains essential amounts of Fe (7.9-9.0 wt% Fe_2O_3), Th (1.0-8.7 wt% ThO_2), Ta (0.5-5.3 wt% Ta_2O_5), REE (2.1-5.0 wt% REE_2O_3) and minor U (0.1-1.9 wt% UO_2). As expected, Ti shows a negative correlation with Nb+Ta and Fe (Figure 3a, c), and Ca apfu values negatively correlate with REE (Figure 3b).

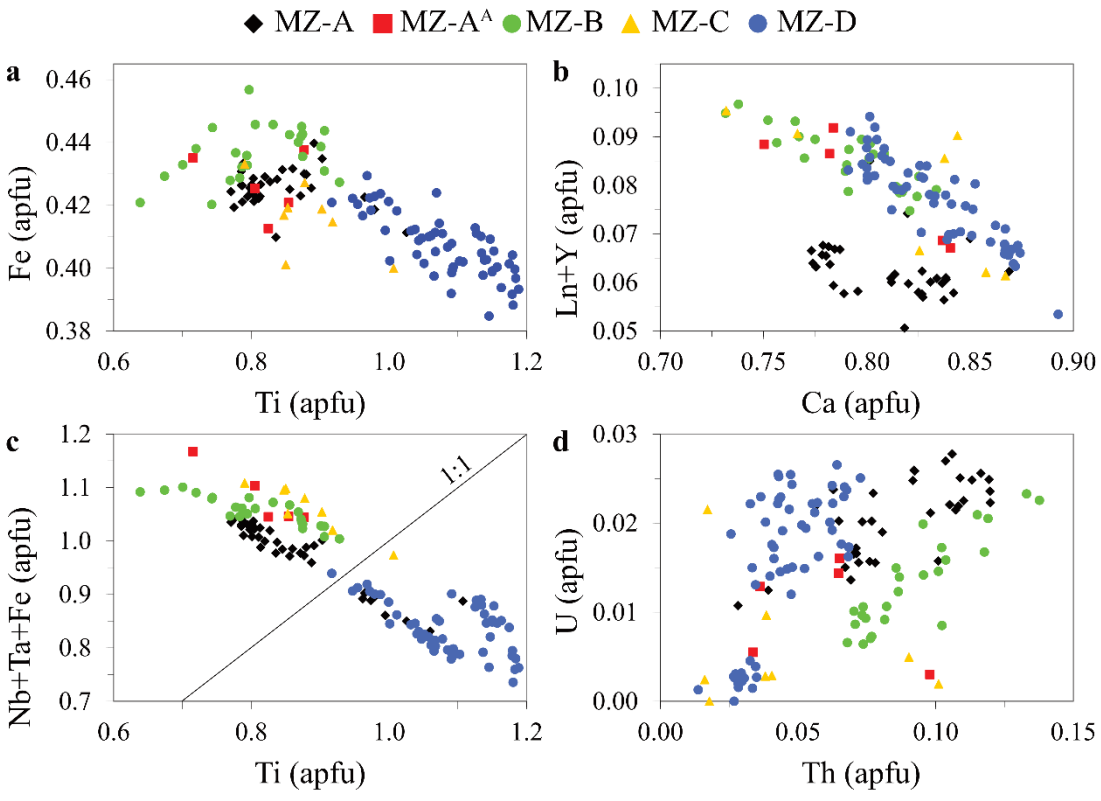

Figure 3. Compositional variations of zirconolite, apfu - atoms per formula unit.

The strong enrichment of carbonatitic zirconolite in Nb and Fe has been discussed by Sharygin *et al.*, (2016) in their study of Fe-Nb-rich zirconolite from Belaya Zima calcite carbonatites. They suggested that such a mineral variety is typical for intrusive carbonatites, and a new mineral, within the zirconolite group, with the

https://doi.org/10.1180/mgm.2024.105 Published online by Cambridge University Press

ideal formula $CaZr(TiNb_{0.5}Fe^{3+}_{0.5})O_7$ (might also be written as $Ca_2Zr_2(Ti_2Nb)FeO_{14}$) could be established. In fact, in the studied zirconolite Ti is the dominant component in only 61 of 128 spot analyses (Figure 3c).

The composition of zirconolite from the studied localities at Kovdor (southern carbonatites and southwestern phoscorites + carbonatites) and groups (MZ-A, A^A, B, C and D) partly overlap (Figure 3). There are, however, some differences in compositions. For example, zirconolite (groups MZ-A, B and C) is enriched in Nb, Ta and Fe and depleted in Th (Figure 3d) compared to those from group MZ-D; data points for zirconolite group MZ-A form a distinct field on Ca *vs* REE plot.

The alteration of zirconolite (group MZ-D, Table 2, 10 spot analyses) led to the mineral enrichment in Si (up to 9.2 wt% SiO_2), Ba (up to 2.9 wt% BaO), Sr (up to 2.6 wt% SrO), Al (up to 1.0 wt% Al_2O_3), and rarely P (3.4 wt% P_2O_5 in single spot analysis). The content of CaO, ZrO_2 and Fe_2O_3 are decreasing (up to 1.7, 17.8 and 1.5 wt% respectively). Analytical totals are low and range between 89.7 and 96.1 wt%.

Composition of the heat-treated zirconolite

Selected zirconolite composition and calculated atoms per formula units (apfu) values are presented in Table 3. The compositional zoning in MZ-A, i.e. RZ-A, is significantly eliminated after heating (Figure 4). Microcrystals of zirconolite can be observed in an enlarged BSE image of RZ-A (Figure 5a), where a set of unoriented dark crystals are formed within a brighter matrix. The darker crystals (2-5 μm) in Figure 5a exhibit lower U, REE, and higher Mg, Fe content (Table 3, point 861-862).

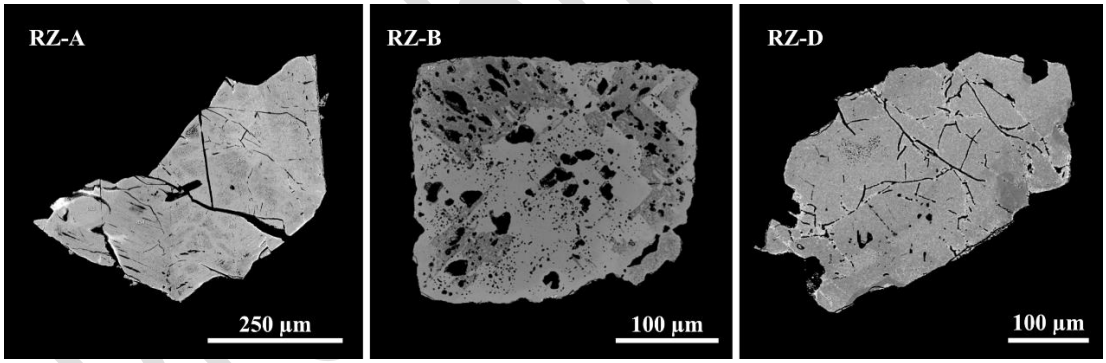

Figure 4. Selected grains of RZ samples, obtained by heating metamict zirconolite in air at 1200 °C for 10 hours. The compositional zoning in RZ-A and RZ-D is significantly eliminated after heating. The intergrowth texture of zirconolite in pyrochlore persists after heating in RZ-B.

The intergrowth texture of zirconolite in pyrochlore persists after heating, as illustrated in Figure 4. The crystallized zirconolite in RZ-B, akin to RZ-A, manifests a prolonged form with a crystal size in the range of 2-5 μm. Other phases are also detected (Table 3; Figure 5b,c), including: srilankite, pyrochlore, baddeleyite and zircon.

https://doi.org/10.1180/mgm.2024.105 Published online by Cambridge University Press

The microcrystals of zirconolite can be identified in RZ-D, where compositional zoning is also eliminated after heating. The redistribution of elements in thus formed crystallites cannot be studied in detail because of the limitations of the microprobe analysis. Brighter phases congregate around cracks and display lower Fe and higher U content.

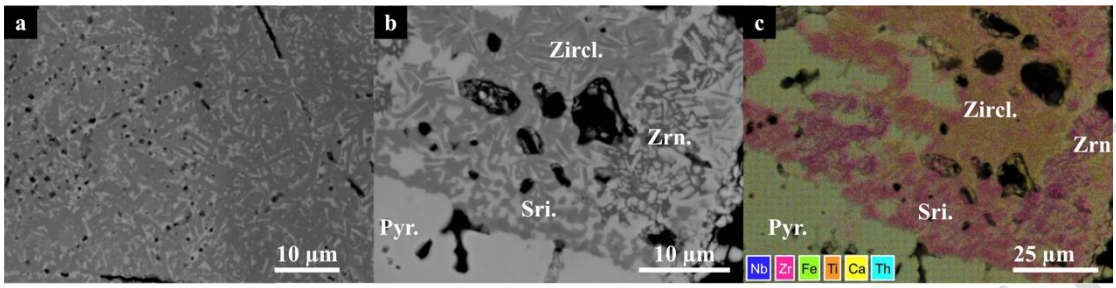

Figure 5. Dark crystals within a brighter matrix of zirconolite composition are observed in sample RZ-A (a). Zirconolite, zircon, and srilankite crystallized within pyrochlore in sample RZ-B (b). The element mapping of the selected region is presented in (c). The chemical composition is given in Table 3.

Raman spectroscopy

Raman spectra of all MZ samples are similar and show the absence of H_2O and $(OH)^-$ (Figure 6a).

Raman spectra of all heat-treated samples are also very similar. RZ-D sample demonstrates a number of sharp and intense Raman bands (Figure 6b). The main peaks are observed at 150, 182, 217, 268, 496, 614 and 767 cm^{-1}, and shoulders at 72, 112, 248, 298, 328, 385, 405, 447, 485, 673, 810 and 861 cm^{-1}. The observed vibrations are in agreement with those previously reported in zirconolite-type minerals (Chukanov *et al.*, 2014, 2018) and synthetic zirconolite (Salamat *et al.*, 2013; Zhang *et al.*, 2018; Blackburn *et al.*, 2020; Thompson *et al.*, 2021). The peak at 770 cm^{-1} is assigned to the symmetric Ti-O vibrations in TiO_6 octahedra. The bands in the range 400–800 cm^{-1} correspond to lower intensity Ti-O internal vibrations, whereas those below 400 cm^{-1} can be attributed to Ca-O and Zr-O vibrations in CaO_8 and ZrO_7 polyhedra (Chukanov *et al.*, 2018; Blackburn *et al.*, 2020). Table 4 lists the peaks observed in RZ-A, RZ-B and RZ-D samples.

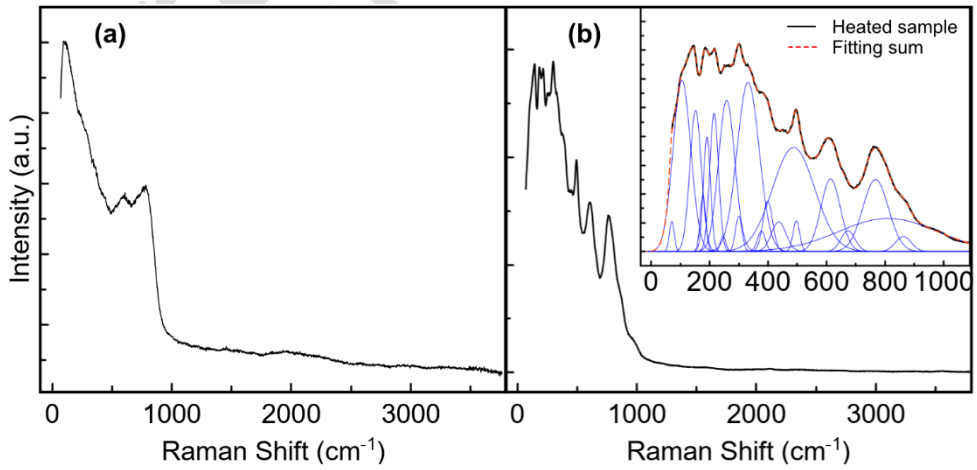

Figure 6. Raman spectra of MZ-D (a) and crystalline RZ-D (b) (laser 532 nm).

https://doi.org/10.1180/mgm.2024.105 Published online by Cambridge University Press

In-situ recrystallization of the metamict zirconolite

Figure 7 shows the evolution of the metamict MZ-D upon heating to 1200 °C. The initial sample contains crystalline hydroxyl apatite inclusions detected via HTPXRD. Upon heating, dehydration of hydroxyapatite occurs, and the decomposition is observed above 750°C. The crystallization of a pyrochlore phase can be identified at 750 °C. A fluorite-type phase starts to crystallize at 420 °C. Table 5 lists the phases identified. The major phases are: zirconolite-3*T* (53 wt%), srilankite (25wt%), pyrochlore (15wt%), baddeleyite (5 wt%) and zircon (3 wt%). This phase identification is in a good agreement with the chemical analyses listed in Table 3.

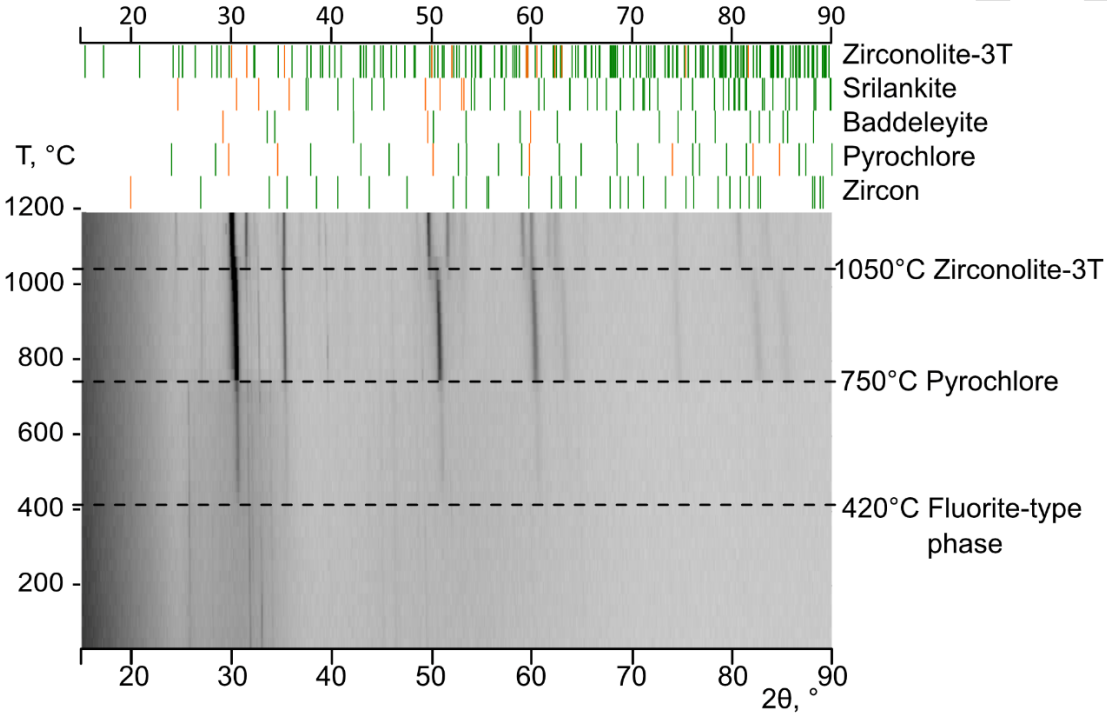

Figure 7. Evolution of MZ-D upon temperature increase. Crystalline hydroxylapatite is present as an impurity in metamict zirconolite. The phase analysis results above are given based on the Rietveld refinement of the cooled sample (see Figure 8).

Zirconolite crystallizes at 1050 °C. Ca is substituted by Th, U, and rare earth elements, while Nb and Ta partially occupy Ti sites. The zirconolite-2*M* is likely to be unstable for the composition with multiple substitutions. Several previous studies have shown the appearance of polytypes such as 3*T*, 3*O*, and 4*M* with increasing levels of substitution in the Ca, Zr, and Ti sites (Gilbert *et al.*, 2010; Ji *et al.*, 2020). The polytype 2*M* is more common for zirconolites with a relatively simple composition and minor substitutions (Vance *et al.*, 2002). The most intense reflection at 2θ = 30.1° is common for all polytypes, leading to a frequently incorrect

https://doi.org/10.1180/mgm.2024.105 Published online by Cambridge University Press

phase identification. Figure 8 compares reflection positions with reference patterns. The observed reflections at 50.2 (220), 59.7 (042), and 60.6 (226) are assigned to zirconolite-3*T*.

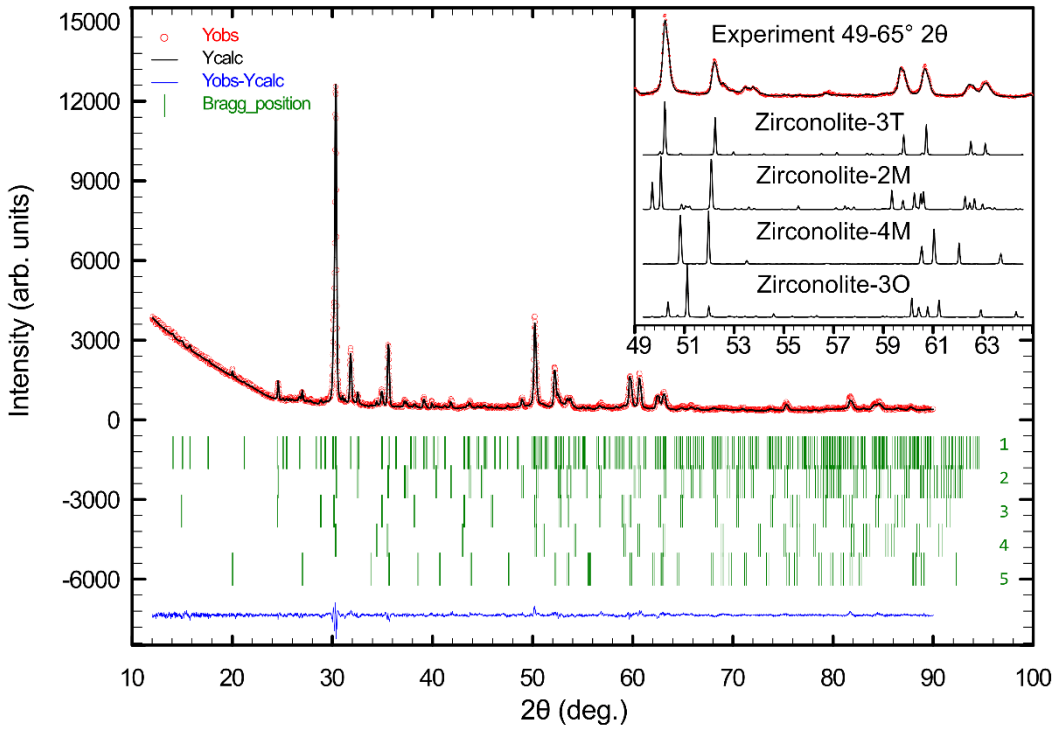

Figure 8. X-ray diffraction pattern of RZ-D. Five identified phases are listed in Table 5, $\chi^2 = 2.19$ indicates a good fit. The inset shows reference patterns for various polytypes and RZ-D (red line) in the range 2θ = 49-65°. Reference patterns used: zirconolite-3*T* (Zubkova *et al.*, 2018), zirconolite-2*M* (Whittle *et al.*, 2012), zirconolite-4*M* (Coelho *et al.*, 1997), and zirconolite-3O (Chukanov *et al.*, 2019).

Thermal expansion of zirconolite-3T

The sample RZ-D was used to examine the thermal expansion of zirconolite-3*T*. Zirconolite-3*T* is very stable upon heating to 1200 °C. *a* unit-cell parameter linearly increases from 7.26 to 7.34 Å, while *c* increases from 16.87 to 17.04 Å (Figure 9).

https://doi.org/10.1180/mgm.2024.105 Published online by Cambridge University Press

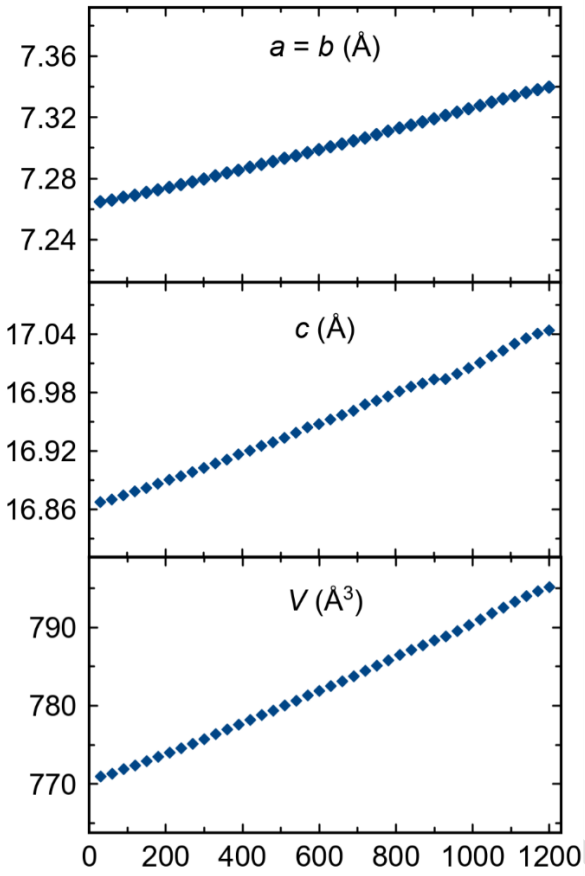

Figure 9. Temperature dependence of unit-cell parameters of zirconolite-3*T*.

Coefficients of thermal expansion (CTE) were obtained by fitting a quadratic polynomial to the temperature dependence of unit-cell parameters in the range 25-1200°C:

$a(T) = b(T) = 7.26240(12) + 0.00005634(47)\times T + 0.00000000737(37)T^2$

$c(T) = 16.86206(78) + 0.0001322(30)\times T + 0.0000000156(24)T^2$

$V(T) = 770.201(41) + 0.01795(16)\times T + 0.00000249(13)T^2$

The CTE values obtained are given in Table 6 and illustrated in Figure 10. The thermal expansion in the *ab* plane is isotropic and constrained by the symmetry. The average CTE values in the temperature range 25-1200 °C are as follows: $\overline{\alpha_a} = \overline{\alpha_b} = \overline{\alpha_{11}} = \overline{\alpha_{22}} = 8.95\cdot10^{-6}$°C^{-1}. Similarly, the thermal expansion along the *c*-axis yields a similar value: $\overline{\alpha_a} = \overline{\alpha_b} = 8.93\cdot10^{-6}$ °C^{-1}, indicating almost isotropic thermal expansion of zirconolite-3*T*.

https://doi.org/10.1180/mgm.2024.105 Published online by Cambridge University Press

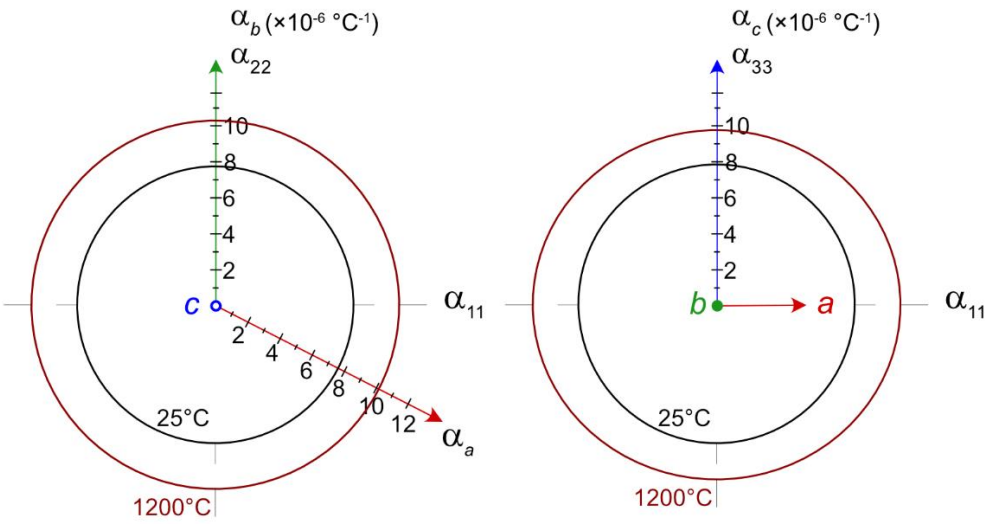

Figure 10. Sections of CTE for zirconolite-3*T*.

Discussion and concluding remarks

At Kovdor, zirconolite occurs in diverse phoscorite and carbonatites. Crystal morphology, internal zoning and mineral composition suggest that, at least, four groups (populations) of zirconolite are present in phoscorites and carbonatites. All studied zirconolite crystals are metamict, and the mineral exhibit notable concentrations of niobium, iron, lanthanides, and actinides.

On heating metamict crystals zirconolite-3*T* crystallizes at 1050°C. The pyrochlore-type and fluorite-type phases precede the crystallization of zirconolite-3*T* (Figure 7). This observation is in agreement with previous studies showing that when the precursor powder with the composition of zirconolite is heated, the first compound formed has a fluorite-type structure (Vance *et al.*, 1990). A reverse sequence of phase evolution was observed for zirconolite damaged by radiation. Ewing and Headley (1983) have reported that upon radiation damage, the crystalline zirconolite first transforms into a mixture of fluorite-type phases, eventually becoming completely amorphous. In addition, the formation of pyrochlore may point to the decomposition of the solid solution of zirconolite. As previous research shows, zirconolite is gradually replaced by pyrochlore, when actinides are present in significant amounts in the Zr-site (Vance *et al.*, 2002; Zhang *et al.*, 2018).

In general, the CTE obtained for the zirconolite-3*T* mineral sample with complex composition agrees well with previous studies. Ball *et al.* (1992) reported CTE values of 10.05(19) ×10^{-6} °C^{-1} and 9.83(15) ×10^{-6} °C^{-1} for 3*T* and 2*M* polytypes, respectively. The lower CTE value observed in our study for zirconolite-3*T* may be attributed to the complex chemistry and polyphase nature of the studied material. It seems that matrix materials may reduce CTE in polyphase ceramics compared to their monophasic counterparts. Zirconolite-3*T* with an almost isotropic thermal expansion confirms the remarkable properties of these phases for the use in complex and multi-component ceramics for the immobilization of HLW.

https://doi.org/10.1180/mgm.2024.105 Published online by Cambridge University Press

Acknowledgments. We thank two anonymous reviewers and Associate Editor Irina Galuskina for many useful remarks that significantly improved initial version of the manuscript. ANZ acknowledges support from The Natural History Museum (London). Technical support by the X-ray diffraction and Geomodel SPbSU Resource Centers is gratefully acknowledged. This work was financially supported by the Russian Science Foundation through the grant 24-63-00006.

Reference

Amelin, Y. and Zaitsev, A.N. (2002) Precise geochronology of phoscorites and carbonatites: The critical role of U-series disequilibrium in age interpretations. *Geochimica et CosmochimicaActa*, **66**, 2399–2419.

Ball, C.J., Thorogood, G.J. and Vance, E.R. (1992) Thermal expansion coefficients of zirconolite ($CaZrTi_2O_7$) and perovskite ($CaTiO_3$) from X-ray powder diffraction analysis. *Journal ofNuclear Materials*, **190**, 298–301.

Bellatreccia, F., Della Ventura, G., Caprilli, E., Williams, C.T. and Parodi, G.C. (1999) Crystal-chemistry of zirconolite and calzirtite from Jacupiranga, São Paulo (Brazil). *Mineralogical Magazine*, **63**, 649–660.

Bellatreccia, F., Ventura, G. Della, Williams, C.T., Lumpkin, G.R., Smith, K.L. and Colella, M. (2002) Non-metamictzirconolitepolytypesfromthefeldspathoid-bearingalkalisyeniticejectaofthe Vico volcanic complex (Latium, Italy). *European Journal of Mineralogy*, **14**, 809–820.

Blackburn, L.R., Sun, S., Gardner, L.J., Maddrell, E.R., Stennett, M.C. and Hyatt, N.C. (2020) A systematic investigation of the phase assemblage and microstructure of the zirconolite $CaZr_{1-x}Ce_xTi_2O_7$ system. *Journal of Nuclear Materials*, **535**, 1–11.

Borodin, L.S., Nazarenko, I.I. and Rikhter, T.L. (1956) On the new mineral zirconolite - a complex AB_3O_7-type oxide. *Doklady Akademii Nauk SSSR*, **110**, 845-848 (in Russian).

Bubnova, R.S., Firsova, V.A., Volkov, S.N. and Filatov, S.K. (2018) *Rietveld to tensor*: program for processing powder x-ray diffraction data under variable conditions.*Glass Physics and Chemistry*, **44**, 33–40.

Bulakh, A.G., Nesterov, A.R. and Williams, C.T. (2006) Zirconolite, $CaZrTi_2O_7$, re-examined from its type locality at Afrikanda, Kola Peninsula, Russia and some Synroc implications. *Neues Jahrbuch für Mineralogie, Abhandlungen*, **182**, 109–121.

Chakhmouradian, A.R. and Williams, C.T. (2004) Mineralogy of high-field-strength elements (Ti, Nb, Zr, Ta, Hf) in phoscoritic and carbonatitic rocks of the Kola Peninsula, Russia. In: *Phoscorites and Carbonatites from Mantle to Mine: The Key Example of the Kola Alkaline Province* (F. Wall and A.N. Zaitsev, editors). Mineralogical Society Series 10, Mineralogical Society, pp. 293-340.

Chakhmouradian, A.R. and Zaitsev, A.N. (1999) Calcite-amphibole-clinopyroxene rock from the Afrikanda

https://doi.org/10.1180/mgm.2024.105 Published online by Cambridge University Press

complex, Kola Peninsula, Russia: mineralogy and a possible link to carbonatites. I. Oxide minerals. *The Canadian Mineralogist*, **37**, 177–198.

Chakhmouradian, A.R. and Zaitsev, A.N. (2002) Calcite-amphibole-clinopyroxene rock from the Afrikanda, Kola Peninsula, Russia: Mineralogy and a possible link to carbonatites. III. Silicate minerals. *The Canadian Mineralogist*, **40**, 1347.

Chakhmouradian, A.R. and Zaitsev, A.N. (2004) Afrikanda: an association of ultramafic, alkaline and alkali-silica-rich carbonatitic rocks from mantle-derived melts. In: *Phoscorites and Carbonatites from Mantle to Mine: The Key Example of the Kola Alkaline Province* (F. Wall and A.N. Zaitsev, editors). Mineralogical Society Series 10, Mineralogical Society, pp. 247-291.

Cheary, R.W. and Coelho, A.A. (1997) A site occupancy analysis of zirconolite $CaZr_xTi_{3-x}O_7$. *Physics and Chemistry of Minerals*, **24**, 447–454.

Chukanov, N. V., Krivovichev, S. V., Pakhomova, A.S., Pekov, I. V., Schäfer, C., Vigasina, M.F. and Van, K. V. (2014) Laachite, $(Ca,Mn)_2Zr_2Nb_2TiFeO_{14}$, a new zirconolite-related mineral from the Eifel volcanic region, Germany. *European Journal of Mineralogy*, **26**, 103–111.

Chukanov, N. V., Zubkova, N. V., Britvin, S.N., Pekov, I. V., Vigasina, M.F., Schäfer, C., Ternes, B., Schüller, W., Polekhovsky, Y.S., Ermolaeva, V.N. and Pushcharovsky, D.Y. (2018) Nöggerathite-(Ce), $(Ce,Ca)_2Zr_2(Nb,Ti)(Ti,Nb)_2Fe^{2+}O_{14}$, a new zirconolite-related mineral from the eifel volcanic region, Germany. *Minerals*, **8**, 1–14.

Chukanov, N. V, Zubkova, N. V, Pekov, I. V, Vigasina, M.F., Polekhovsky, Y.S., Ternes, B., Schüller, W., Britvin, S.N. and Pushcharovsky, D.Yu. (2019) Stefanweissite, $(Ca,REE)_2Zr_2(Nb,Ti)(Ti,Nb)_2Fe^{2+}O_{14}$, a new zirconolite-related mineral from the Eifel paleovolcanic region, Germany. *Mineralogical Magazine*, **83**, 607–614.

Coelho, A.A., Cheary, R.W. and Smith, K.L. (1997) Analysis and Structural Determination of Nd-Substituted Zirconolite-4M. *Journal of Solid State Chemistry*, **129**, 346–359.

Downes, H., Balaganskaya, E., Beard, A., Liferovich, R. and Demaiffe, D. (2005) Petrogenetic processes in the ultramafic, alkaline and carbonatitic magmatism in the Kola Alkaline Province: A review. *Lithos*, **85**, 48–75.

Ewing, R.C. and Headley, T.J. (1983) Alpha-recoil damage in natural zirconolite ($CaZrTi_2O_7$). *Journal of Nuclear Materials*, **119**, 102–109.

Gieré, R., Williams, C.T. and Lumpkin, G.R. (1998) Chemical characteristics of natural zirconolite. *Schweizerische Mineralogische und Petrographische Mitteilungen***78**, 433–459.

Gilbert, M.R., Selfslag, C., Walter, M., Stennett, M.C., Somers, J., Hyatt, N.C. and Livens, F.R. (2010) Synthesis and characterisation of Pu-doped zirconolites –$(Ca_{1-x}Pu_x)Zr(Ti_{2-2x}Fe_{2x})O_7$. *IOP Conference Series: Materials Science and Engineering*, **9**, 012007.

Grey, I.E., Mumme, W.G., Ness, T.J., Roth, R.S. and Smith, K.L. (2003) Structural relations between weberite

https://doi.org/10.1180/mgm.2024.105 Published online by Cambridge University Press

and zirconolite polytypes—refinements of doped 3T and 4M $Ca_2Ta_2O_7$ and 3T $CaZrTi_2O_7$. *Journal of Solid State Chemistry*, **174**, 285–295.

Hazen, R.M., Finger, L.W., Agrawal, D.K., McKinstry, H.A. and Perrotta, A.J. (1987) High-temperature crystal chemistry of sodium zirconium phosphate (NZP). *Journal of Materials Research*, **2**, 329–337.

Hunter, B.A., Howard, C.J. and Kim, D.-J. (1998) Neutron diffraction study of tetragonal zirconias containing tetravalent dopants. *Australian Journal of Physics*, **51**, 539–545.

Ivanyuk, G.Yu., Yakovenchuk, V.N. and Pakhomovsky, Ya.A. (2002) Kovdor. Laplandia minerals, Apatity, 326 p.

Ivanyuk, G.Yu., Kalashnikov, A.O., Pakhomovsky, Ya.A., Mikhailova, J.A., Yakovenchuk, V.N., Konopleva, N.G., Sokharev, V.A., Bazai, A. V and Goryainov, P.M. (2016) Economic minerals of the Kovdor baddeleyite-apatite-magnetite deposit, Russia: mineralogy, spatial distribution and ore processing optimization. *Ore Geology Reviews*, **77**, 279–311.

Ji, S., Su, M., Liao, C., Ma, S., Wang, Z., Shih, K., Chang, C.K., Lee, J.F., Chan, T.S. and Li, Y. (2020) Synchrotron x-ray spectroscopy investigation of the $Ca_{1-x}Ln_xZrTi_{2-x}(Al, Fe)_xO_7$ zirconolite ceramics (Ln=La, Nd, Gd, Ho, Yb). *Journal of the American Ceramic Society*, **103**, 1463–1475.

Ji, S., Liao, C.-Z., Chen, S., Zhang, K., Shih, K., Chang, C.-K., Sheu, H., Yan, S., Li, Y. and Wang, Z. (2021) Higher valency ion substitution causing different fluorite-derived structures in $CaZr_{1-x}Nd_xTi_{2-x}Nb_xO_7$ ($0.05 \leq x \leq 1$) solid solution. *Ceramics International*, **47**, 2694–2704.

Kapustin, Yu.L. (1980) Mineralogy of Carbonatites. Amerind Publishing, New Dehli, 259 p.

Kessoft, S.E., Sinclair, W.J. and Ringwood, A.E. (1983) Solid solution limits in synroc zirconolite. *Nuclear and Chemical Waste Management*, **4**, 259–265.

Kirillov, A.S. and Burova, T.A. (1967) Lueshites from Kola peninsula carbonatites. *Mineralogy and Geochem*istry **II**, 28–39 (In Russian).

Krasnova, N.I., Balaganskaya, E.G. and Garcia, D. (2004) Kovdor - classic phoscorites and carbonatites. In: *Phoscorites and Carbonatites from Mantle to Mine: The Key Example of the Kola Alkaline Province* (F. Wall and A.N. Zaitsev, editors). Mineralogical Society Series 10, Mineralogical Society, pp. 99-132.

Kukharenko, A.A., Orlova, M.P., Bulakh, A.G., Bagdasarov, E.A., Rimskaya-Korsakova, O.M., Nefedov, E.I., Ilingsky, G.A., Sergeev, A.S. and Abakumova, N.B. (1965) *The Caledonian complex of ultramafic, alkaline rocks and carbonatites of the Kola Peninsula and Northern Karelia.* Nedra, Leningrad, 772 p. (in Russian).

Lewandowski, J.T., Pickering, I.J. and Jacobson, A.J. (1992) *Hydrothermal synthesis of calcium - niobium and tantalum oxides with the pyrochlore structure*. Materials Research Bulletin, 27, 981–988.

Lutze, W. and Ewing, R.C. (Editors) (1988) *Radioactive Waste Forms for the Future*. North-Holland, Amsterdam, 778 pp.

Osokin, A.S. (1979) Accessory-rare-metal mineralization in carbonatites of one alkali-ultramafic massif (Kola

https://doi.org/10.1180/mgm.2024.105 Published online by Cambridge University Press

Peninsula). *Mineralogy and Geochemistry*, **6**, 27-38 (in Russian).

Pascal, M.-L., Di Muro, A., Fonteilles, M. and Principe, C. (2009) Zirconolite and calzirtite in banded forsterite-spinel-calcite skarn ejecta from the 1631 eruption of Vesuvius: inferences for magma-wallrock interactions. *Mineralogical Magazine*, **73**, 333–356.

Rimskaya-Korsakova, O.M., Burova, T.A. and Frank-Kamenetskiy, V.A. (1963)Lueshitefrom carbonatites of the Kovdor massif. *ZapiskiVsesoyuznogoMineralogicheskogoObschestva*,**92**, 173-183 (in Russian).

Salamat, A., McMillan, P.F., Firth, S., Woodhead, K., Hector, A.L., Garbarino, G., Stennett, M.C. and Hyatt, N.C. (2013) Structural transformations and disordering in zirconolite ($CaZrTi_2O_7$) at high pressure. *Inorganic Chemistry*, **52**, 1550–1558.

Sameera, S., Prabhakar Rao, P. and Chandran, M.R. (2011) Structure and dielectric properties of a new series of pyrochlores in the Ca-Sm-Ti-M-O (M = Nb and Ta) system. *Journal of Materials Science: Materials in Electronics*, **22**, 1631–1636.

Sharygin, V. V., Doroshkevich, A.G. and Khromova, E.A. (2016) Nb-Fe-rich zirconolite-group minerals in calcite carbonatites of the Belaya Zima massif (Eastern Sayan) *Mineralogy*, **4**, 3–18 (in Russian).

Siggel, A. and Jansen, M. (1990) $ZrSn_{0,5}Ti_{0,5}O4$ als Wirtsstruktur für keramische Farbkörper Strukturuntersuchungen an $ZrTiO_4$ und $ZrSn_{0,5}Ti_{0,5}O_4$. *Zeitschrift für anorganische und allgemeine Chemie*, **582**, 93–102(in German).

Strelnikova, L.A. and Polezhaeva, L.I. (1981) Accessory minerals of the pyrochlore group from carbonatites of some alkali-ultramafic massifs. *Composition of Alkaline Intrusive Complexes of the Kola Peninsula*. Kola Branch of the USSRAcademy of Sciences, Apatity. 81-88 (in Russian).

Subbotin, V. V. and Subbotina, G.F. (2000) Minerals of the pyrochlore group in phoscorites and carbonatites of the Kola Peninsula (in Russian). *Vestnik of MSTU*, **3**, 273–284 (in Russian).

Thompson, N.B.A., Frankland, V.L., Bright, J.W.G., Read, D., Gilbert, M.R., Stennett, M.C. and Hyatt, N.C. (2021) The thermal decomposition of studtite: analysis of the amorphous phase. *Journal of Radioanalytical and Nuclear Chemistry*, **327**, 1335–1347.

Vance, E.R., Ball, C.J., Blackford, M.G., Cassidy, D.J. and Smith, K.L. (1990) Crystallisation of zirconolite from an alkoxide precursor. *Journal of Nuclear Materials*, **175**, 58–66.

Vance, E.R., Lumpkin, G.R., Carter, M.L., Cassidy, D.J., Ball, C.J., Day, R.A. and Begg, B.D. (2002) Incorporation of uranium in zirconolite ($CaZrTi_2O_7$). *Journal of the American Ceramic Society*, **85**, 1853–1859.

Della Ventura, G. Della, Bellatreccia, F. and Williams, C.T. (2000) Zirconolite with significant *REE*ZrNb(Mn,Fe)O_7 from a xenolith of the Laacher See eruptive center, Eifel volcanic region, Germany. *Canadian Mineralogist*, **38**, 57–65.

Whittle, K.R., Hyatt, N.C., Smith, K.L., Margiolaki, I., Berry, F.J., Knight, K.S. and Lumpkin, G.R. (2012) Combined neutron and X-ray diffraction determination of disorder in doped zirconolite-2M. *American*

https://doi.org/10.1180/mgm.2024.105 Published online by Cambridge University Press

Mineralogist, **97**, 291–298.

Williams, C.T. (1996) The occurrence of niobian zirconolite, pyrochlore and baddeleyite in the Kovdor carbonatite complex, Kola Peninsula, Russia. *Mineralogical Magazine*, **60**, 639–646.

Williams, C.T. and Gieré, R. (1996) Zirconolite: A review of localities worldwide, and a compilation of its chemical compositions. *Bulletin of the NaturalHistoryMuseum,London*, **52**, 1–24.

Wu, F.Y., Yang, Y.H., Mitchell, R.H., Bellatreccia, F., Li, Q.L. and Zhao, Z.F. (2010) In-situ U-Pb and Nd-Hf-(Sr) isotopic investigations of zirconolite and calzirtite. *Chemical Geology*, **277**, 178–195.

Yudintsev, S. V., Nickolsky, M.S., Ojovan, M.I., Stefanovsky, O.I., Nikonov, B.S. and Ulanova, A.S. (2022) Zirconolite polytypes and murataitepolysomes in matrices for the REE-Actinide fraction of HLW. *Materials*, **15**, 6091.

Zaitsev, A.N. and Chakhmouradian, A.R. (2002) Calcite-amphibole-clinopyroxene rock from the Afrikanda complex, Kola Peninsula, Russia: mineralogy and a possible link to carbonatites. II. Oxysalt minerals. *The Canadian Mineralogist*, **40**, 103–120.

Zaitsev, A.N., Terry Williams, C., Jeffries, T.E., Strekopytov, S., Moutte, J., Ivashchenkova, O. V, Spratt, J., Petrov, S. V, Wall, F., Seltmann, R. and Borozdin, A.P. (2015) Rare earth elements in phoscorites and carbonatites of the Devonian Kola Alkaline Province, Russia: Examples from Kovdor, Khibina, Vuoriyarvi and Turiy Mys complexes. *Ore Geology Reviews*, **64**, 477–498.

Zaitsev, A.N., Zhitova, E.S., Spratt, John, Zolotarev, A.A. and Krivovichev, S.V. (2017) Isolueshite, $NaNbO_3$, from the Kovdor carbonatite, Kola peninsula, Russia: composition, crystal structure and possible formation scenarios. *NeuesJahrbuchfürMineralogie - Abhandlungen* Band 194, Heft 2, 165-173.

Zhang, Y.B., Wang, J., Wang, J.X., Huang, Y., Luo, P., Liang, X.F. and Tan, H. Bin. (2018) Phase evolution, microstructure and chemical stability of $Ca_{1-x}Zr_{1-x}Gd_{2x}Ti_2O_7$ ($0.0 \leq x \leq 1.0$) system for immobilizing nuclear waste. *Ceramics International*, **44**, 13572–13579.

Zubkova, N. V, Chukanov, N. V, Pekov, I. V, Ternes, B., Schüller, W., Ksenofontov, D.A. and Pushcharovsky, D.Yu. (2018) The crystal structure of nonmetamict Nb-rich zirconolite-3*T* from the Eifel paleovolcanic region, Germany. *Zeitschrift für Kristallographie - Crystalline Materials*, **233**, 463–468.

https://doi.org/10.1180/mgm.2024.105 Published online by Cambridge University Press

Table 1. Selected compositions of metamict zirconolite.

Type	MZ-A				MZ-A1		MZ-B				
Sample	65/a		04850		421		1066/4		1066/3	208/12	
Position	core	core	core	rim			core	rim	rim	core	
Point	1	6	37	39	60	61	29	30	82	91	115
Na_2O						0.17			0.14	0.07	
MgO	0.82	0.73	0.50	0.30	0.48	0.73	0.53	0.47	0.36	1.17	0.67
Al_2O_3	0.18	0.16	0.08	0.10						0.20	0.11
CaO	10.60	10.90	11.48	12.79	12.18	11.12	11.30	11.63	11.70	9.85	11.17
TiO_2	15.39	17.03	19.67	22.23	18.18	14.46	16.70	17.71	18.20	12.14	15.77
MnO	0.51	0.48	0.34	0.22	0.24	0.32	0.49	0.50	0.40	0.70	0.52
Fe_2O_3	8.36	8.45	8.51	8.50	8.97	8.69	8.85	8.87	8.75	7.90	8.49
Y_2O_3	0.13	0.13	0.17	0.17	0.16	0.13	0.14	0.13	0.14	0.12	0.14
ZrO_2	30.39	30.26	32.00	33.92	31.49	29.34	29.52	29.96	29.19	29.31	30.02
Nb_2O_5	15.68	15.73	14.93	13.59	20.71	24.05	19.46	18.64	18.22	19.12	18.62
La_2O_3	0.25	0.24	0.34	0.30	0.32	0.39	0.35	0.32	0.33	0.33	0.34
Ce_2O_3	1.04	0.97	1.41	0.98	1.11	1.64	1.46	1.30	1.36	1.60	1.43
Pr_2O_3	0.20	0.11	0.24	0.15	0.18	0.27	0.22	0.23	0.26	0.28	0.23
Nd_2O_3	0.69	0.67	1.01	0.72	0.79	1.00	1.13	0.96	1.01	1.10	1.00
Sm_2O_3	0.15	0.15	0.20	0.21	0.18	0.22	0.21	0.20	0.18	0.23	0.21
Gd_2O_3	0.09	0.11	0.15	0.12	0.16	0.14	0.12	0.13	0.09	0.09	0.11
HfO_2	0.38	0.43	0.53	0.56	0.61	0.50	0.25	0.29	0.31	0.33	0.33
Ta_2O_5	5.35	4.46	2.51	2.10	0.66	1.23	2.73	2.91	2.91	3.75	3.27
ThO_2	7.73	6.88	4.24	1.95	2.31	4.32	5.07	4.95	4.70	8.65	5.70
UO_2	1.47	1.48	1.64	0.76	0.39	0.98	0.48	0.44	0.69	1.45	0.94
Total	99.52[1]	99.37	99.96	99.66	99.12	99.71	99.06[2]	99.60	98.93	98.54[3]	99.08
Structural formulae calculated on the basis of 7O											
Ca	0.774	0.784	0.801	0.869	0.837	0.784	0.802	0.816	0.825	0.738	0.801
Th	0.120	0.105	0.063	0.028	0.034	0.065	0.076	0.074	0.070	0.138	0.087
U	0.022	0.022	0.024	0.011	0.005	0.014	0.007	0.006	0.010	0.023	0.014
Y	0.005	0.005	0.006	0.006	0.005	0.005	0.005	0.004	0.005	0.005	0.005
La	0.006	0.006	0.008	0.007	0.008	0.010	0.009	0.008	0.008	0.009	0.008
Ce	0.026	0.024	0.034	0.023	0.026	0.039	0.035	0.031	0.033	0.041	0.035
Pr	0.005	0.003	0.006	0.003	0.004	0.007	0.005	0.005	0.006	0.007	0.006
Nd	0.017	0.016	0.024	0.016	0.018	0.024	0.027	0.023	0.024	0.027	0.024
Sm	0.004	0.004	0.005	0.004	0.004	0.005	0.005	0.005	0.004	0.006	0.005
Gd	0.002	0.002	0.003	0.003	0.003	0.003	0.003	0.003	0.002	0.002	0.002
Na						0.021			0.018	0.009	
Total	0.982[1]	0.970	0.973	0.970	0.944	0.976	0.974[2]	0.974	1.005	1.006[3]	0.987
Zr	1.009	0.99	1.017	1.048	0.984	0.941	0.953	0.957	0.9	0.999	0.980

https://doi.org/10.1180/mgm.2024.105 Published online by Cambridge University Press

		0							37		
Hf	0.007	0.008	0.010	0.010	0.011	0.009	0.005	0.005	0.006	0.007	0.006
Total	1.017	0.999	1.027	1.058	0.996	0.950	0.958	0.962	0.943	1.006	0.986
Ti	0.789	0.860	0.965	1.060	0.877	0.716	0.832	0.872	0.901	0.639	0.794
Nb	0.483	0.477	0.440	0.389	0.600	0.715	0.582	0.552	0.542	0.604	0.563
Fe^{3+}	0.429	0.427	0.418	0.405	0.433	0.430	0.441	0.437	0.434	0.416	0.428
Ta	0.099	0.081	0.045	0.036	0.012	0.022	0.049	0.052	0.052	0.071	0.060
Mg	0.084	0.073	0.048	0.028	0.046	0.071	0.052	0.046	0.035	0.122	0.067
Mn	0.030	0.027	0.018	0.012	0.013	0.018	0.028	0.028	0.022	0.041	0.030
Total	1.912	1.946	1.934	1.931	1.980	1.972	1.983	1.986	1.987	1.894	1.941

Including (1) 0.11 wt% PbO (0.002 apfu), (2) 0.04 wt% PbO (0.001 apfu), (3) 0.13 wt% PbO (0.002 apfu). Si, K, P, Sr, Ba, Dy, Er, Yb, W, F and Cl – below detection limit. Blanks in the Table – content of the element is below detection limit.

Table 1. (Continued.)

Type	MZ-C			MZ-D							
Sample	04774			4 (2)				10c/534			
Position	core	core	rim	core		rim	rim	core	mantle		rim
Point	139	145	146	163	166	151	155	50	57	59	60
Na_2O	0.11	0.19	0.27								0.08
MgO	0.75	0.44	0.35	0.45	0.40	0.18	0.10	0.47	0.45	0.39	0.17
Al_2O3				0.09	0.08	0.14	0.11	0.06		0.07	0.06
CaO	10.66	12.68	12.63	11.71	11.69	12.27	13.12	11.73	11.66	11.97	12.91
TiO_2	15.66	18.80	21.12	21.99	22.81	24.78	24.59	19.85	19.90	20.46	23.27
MnO	0.30	0.19	0.21	0.25	0.26	0.21	0.25	0.33	0.29	0.32	0.31
Fe_2O_3	8.48	8.61	8.28	8.10	8.21	8.09	8.42	8.70	8.49	8.52	8.59
Y_2O_3	0.16	0.11	0.10	0.18	0.19	0.21	0.21	0.15	0.15	0.16	0.17
ZrO_2	28.54	30.39	30.35	33.74	32.89	31.72	31.29	31.68	31.82	32.01	30.81
Nb_2O_5	21.10	19.44	18.24	12.45	12.22	11.78	15.81	15.52	15.08	14.75	17.22
La_2O_3	0.31	0.24	0.28	0.36	0.37	0.35	0.29	0.33	0.30	0.36	0.33
Ce_2O_3	1.39	0.97	1.05	1.46	1.38	1.22	1.02	1.25	1.23	1.22	1.15
Pr_2O_3	0.24	0.16	0.21	0.23	0.22	0.19	0.12	0.23	0.27	0.24	0.16
Nd_2O_3	1.18	0.83	0.82	1.08	1.21	0.97	0.89	1.03	0.96	0.94	0.91
Sm_2O_3	0.27	0.18	0.21	0.23	0.26	0.21	0.19	0.19	0.21	0.20	0.16
Gd_2O_3	0.14	0.12		0.14	0.14	0.15	0.14	0.13	0.15	0.12	0.13
HfO_2	0.43	0.58	0.66	0.44	0.45	0.35	0.28	0.50	0.42	0.45	0.32
Ta_2O_5	2.20	4.59	3.24	2.22	2.03	2.01	0.59	2.24	2.09	2.06	0.76
ThO_2	5.91	1.23	1.12	2.98	3.62	3.17	1.91	4.46	4.59	3.89	2.36
UO_2	0.33		0.17	1.60	1.36	1.05	0.19	1.22	1.12	1.13	0.11
Total	98.15	99.7	99.31	99.71	99.78	99.04	99.49	100.06	99.1	99.25	100.08[1]

https://doi.org/10.1180/mgm.2024.105 Published online by Cambridge University Press

		5							8		
Structural formulae calculated on the basis of 7O											
Ca	0.766	0.867	0.858	0.808	0.805	0.838	0.874	0.815	0.817	0.833	0.862
Th	0.090	0.018	0.016	0.044	0.053	0.046	0.027	0.066	0.068	0.057	0.033
U	0.005		0.002	0.023	0.019	0.015	0.003	0.018	0.016	0.016	0.001
Y	0.006	0.004	0.003	0.006	0.007	0.007	0.007	0.005	0.005	0.006	0.006
La	0.008	0.006	0.007	0.009	0.009	0.008	0.007	0.008	0.007	0.009	0.008
Ce	0.034	0.023	0.024	0.034	0.032	0.028	0.023	0.030	0.029	0.029	0.026
Pr	0.006	0.004	0.005	0.005	0.005	0.004	0.003	0.006	0.006	0.006	0.004
Nd	0.028	0.019	0.018	0.025	0.028	0.022	0.020	0.024	0.022	0.022	0.020
Sm	0.006	0.004	0.005	0.005	0.006	0.005	0.004	0.004	0.005	0.004	0.004
Gd	0.003	0.003		0.003	0.003	0.003	0.003	0.003	0.003	0.003	0.003
Na	0.014	0.023	0.033								0.010
Total	0.967	0.970	0.972	0.963	0.967	0.977	0.970	0.977	0.980	0.984	0.979[1]
Zr	0.934	0.946	0.938	1.060	1.031	0.986	0.948	1.001	1.014	1.013	0.937
Hf	0.008	0.011	0.012	0.008	0.008	0.006	0.005	0.009	0.008	0.008	0.006
Total	0.942	0.957	0.950	1.068	1.039	0.992	0.953	1.011	1.022	1.022	0.942
Ti	0.790	0.903	1.007	1.066	1.103	1.188	1.150	0.968	0.979	1.000	1.091
Nb	0.640	0.561	0.522	0.362	0.355	0.339	0.444	0.455	0.446	0.433	0.485
Fe3+	0.428	0.414	0.395	0.392	0.397	0.388	0.394	0.424	0.418	0.416	0.403
Ta	0.040	0.080	0.056	0.039	0.036	0.035	0.010	0.040	0.037	0.036	0.013
Mg	0.075	0.042	0.033	0.044	0.038	0.017	0.009	0.045	0.044	0.038	0.016
Mn	0.017	0.010	0.011	0.013	0.014	0.011	0.013	0.018	0.016	0.017	0.016
Total	1.991	2.010	2.024	1.917	1.943	1.979	2.021	1.950	1.939	1.940	2.024

Including (1) 0.10wt% Dy_2O_3 (0.002 apfu). Si, K, P, Sr, Ba, Pb, Er, Yb, W, F and Cl – below detection limit. Blanks in the Table – content of the element is below detection limit.

https://doi.org/10.1180/mgm.2024.105 Published online by Cambridge University Press

Table 2. Selected compositions of altered zirconolite.

Type	MZ-D					
Sample						
Position			core	rim	rim	rim
Point	14	43	161	27	158	182
Na_2O	0.08		0.17			0.60
MgO	0.10	0.06	0.10	0.34	0.06	0.16
Al_2O_3	0.09	0.10	0.09	1.05		
SiO_2	0.22	0.47		8.27	9.21	3.35
P_2O_5				3.37		
K_2O	0.13		0.16	0.12	0.20	0.16
CaO	7.78	9.44	2.45	3.46	3.22	6.90
TiO_2	25.40	24.02	23.24	19.98	19.68	19.24
MnO	0.21	0.23	0.23		0.11	0.30
Fe_2O_3	4.31	5.59	2.44	3.74	1.52	5.06
SrO	0.14	0.11	0.46	0.19	2.58	0.07
Y_2O_3	0.16	0.18	0.16	0.10		0.17
ZrO_2	31.32	30.70	36.12	17.78	27.03	29.56
Nb_2O_5	18.31	16.03	13.91	22.12	16.26	14.86
BaO			0.55	1.70	2.92	0.18
La_2O_3	0.31	0.28	0.36	0.27	0.24	0.29
Ce_2O_3	0.99	0.99	1.49	0.65	0.94	1.14
Pr_2O_3	0.15	0.14	0.08			0.12
Nd_2O_3	0.80	0.82	1.13	0.33	0.76	0.85
Sm_2O_3	0.15	0.20	0.17			0.18
Gd_2O_3	0.09	0.11	0.16		0.09	0.12
HfO_2	0.35	0.30	0.47	0.30	0.29	0.28
Ta_2O_5	0.61	0.54	2.39	2.65	2.42	3.18
ThO_2	2.26	2.47	2.93	3.04	4.19	4.65
UO_2	0.43	0.37	1.84	0.29	1.19	1.74
Total	94.38	93.15	91.11	89.74	92.93	93.15

Dy, Er, Yb, W, F and Cl – below detection limit. Blanks in the Table – content of the element is below detection limit.

Table 3. Selected compositions of recrystallized zirconolite, pyrochlore, srilankite and zircon, which were analyzed using Hitachi SEM.

https://doi.org/10.1180/mgm.2024.105 Published online by Cambridge University Press

	RZ-A			RZ-B				RZ-D		
	Zirconolite			Pyrochlore	Zirconolite	Srilankite	Zircon	Zirconolite		Zircon
Ideal formula	ABM_2O_7			$A_2M_2O_7$	ABM_2O_7	$ZrTiO_4$	$ZrSiO_4$	ABM_2O_7		$ZrSiO_4$
Position		Crystals	Matrix			Crystals		Cracks	Matrix	Cracks
Colour BSE		Dark	Bright	Bright	Grey	Grey	Dark	Bright	Grey	Dark
Point	850	861	862	881	882	888	890	994	1003	1027
Na_2O		0.22			0.14	0.13			0.15	
MgO	0.78	0.7	0.41	0.28	0.56	0.46			0.18	
Al_2O_3	0.16	0.14	0.2	0.12	0.2	0.24	0.24	0.22	0.33	
SiO_2				1.1	0.65	0.35	24.31	0.91		28.15
CaO	11.33	11.97	9.2	15.22	10.29	4.54	3.72	8.7	13.52	1.69
TiO_2	15.47	18.55	12.74	15.36	16.95	17.29	4.42	23.6	26.56	3.35
ZrO_2	30.27	29.84	39.22	3.01	28.63	38.53	45.41	28.92	30.52	56.21
Nb_2O_5	17.78	15.7	15.41	30.26	17.2	18.52	6.66	19.31	15.22	3.79
La_2O_3	0.75			1.32	0.65	0.68	0.49	0.75	0.88	
Ce_2O_3	1.09	0.93	1.3	2.52	1.04	0.98	0.91	2.15	1.01	0.73
Nd_2O_3	0.73	0.9	0.8	0.54	1.42	0.46		1.28	1.15	
Sm_2O_3					0.63			0.29		
Gd_2O_3								0.38		
Dy_2O_3							0.39			
Er_2O_3	0.53									
HfO_2							0.83	0.45		0.73
Ta_2O_5	4.82	4.99	4.15	5.21	2.26	2.2		1.86	0.94	
ThO_2	6.03	5.82	6.5	12.82	6.27	3.05	5.62	5.15	2.17	2.79
UO_2	1.95	0.61	1.93	10.53	3.52	3.27	5.73	3.22	0.73	1.61
MnO	0.62	0.45	0.48	0.18	0.62	0.23		0.3	0.47	
Fe_2O_3	7.42	8.97	5.25	1.97	9.02	9.2	1.01	4.32	7.41	0.28
Total	99.73	99.78	97.58	100.45	100.06	100.14	99.74	101.82	101.25	99.34
		Apfu calculated on the basis of *n* O atoms								
Ca	0.818	0.840	0.692	1.162	0.734	0.182	0.134	0.593	0.883	0.058
La	0.019			0.035	0.016	0.010	0.006	0.018	0.020	
Ce	0.027	0.022	0.033	0.066	0.025	0.014	0.011	0.050	0.023	0.009
Nd	0.018	0.021	0.020	0.014	0.034	0.006		0.029	0.025	
Sm					0.014			0.006		
Gd								0.008		
Dy							0.004			
Er	0.011									
Th	0.092	0.087	0.104	0.208	0.095	0.026	0.043	0.074	0.030	0.020
U	0.029	0.009	0.030	0.167	0.052	0.028	0.043	0.046	0.010	0.011
Na		0.028			0.018	0.010			0.018	0.000
Total	1.014	1.007	0.879	1.651	0.988	0.272	0.241	0.824	1.009	0.098
Zr	0.994	0.953	1.342	0.105	0.929	0.700	0.743	0.896	0.908	0.874
Hf							0.008	0.008	0.000	0.007
Total	0.994	0.953	1.342	0.105	0.929	0.700	0.751	0.905	0.908	0.881
Ti	0.784	0.914	0.672	0.823	0.849	0.484	0.112	1.129	1.219	0.080
Si				0.078	0.043	0.014	0.816	0.058		0.898

https://doi.org/10.1180/mgm.2024.105 Published online by Cambridge University Press

Mg	0.078	0.068	0.043	0.030	0.056	0.026			0.016	
Mn	0.035	0.025	0.029	0.011	0.035	0.008	0.000	0.016	0.024	
Fe^{3+}	0.376	0.442	0.277	0.106	0.452	0.258	0.026	0.207	0.340	0.007
Al	0.013	0.011	0.017	0.010	0.016	0.010	0.009	0.016	0.024	
Nb	0.541	0.465	0.489	0.975	0.517	0.312	0.101	0.555	0.420	0.055
Ta	0.088	0.089	0.079	0.101	0.041	0.022		0.032	0.016	
Total	1.916	2.014	1.606	2.134	2.008	1.132	1.064	2.013	2.058	1.040
O=	7	7	7	7	7	4	4	7	7	4

Table 4. Raman shift (cm^{-1}) of bands observed in RZ samples.

RZ-A	RZ-B	RZ-D
76	72	72
96	102	112
139	133	150
183	181	182
204	199	
211		217
249	251	248
266	267	268
297	302	298
329	331	328
346	347	
377	366	385
	409	405
442	446	447
493		485
499	504	496
606	601	
	609	614
657	660	673
780	776	767
		810
861	861	861

https://doi.org/10.1180/mgm.2024.105 Published online by Cambridge University Press

Table 5. Refinement parameters and phases formed upon heating of MZ-D sample.

χ^2	2.19
Rp	3.66
Rwp	4.98
Rexp	3.36

Phase		Wt.%	Reference
1	Zirconolite-3T	53.6(5)	(Zubkova *et al.*, 2018)
2	Srilankite	24.6(4)	(Siggel and Jansen, 1990)
3	Pyrochlore	14.6(2)	(Lewandowski *et al.*, 1992)
4	Baddeleyite	4.98(3)	(Hunter *et al.*, 1998)
5	Zircon	2.25(6)	(Hazen *et al.*, 1987)

Table 6. CTE values* for zirconolite-3*T* from Kovdor.

T, °C	$\alpha_{11}=\alpha_{22}=\alpha_a=\alpha_b$	$\alpha_{33}=\alpha_c$	α_V
25	7.807(62)	7.89(17)	23.50(20)
200	8.151(45)	8.20(12)	24.50(14)
400	8.543(26)	8.555(73)	25.640(85)
600	8.932(15)	8.909(43)	26.773(50)
800	9.319(25)	9.262(68)	27.900(80)
1000	9.704(42)	9.61(12)	29.02(14)
1200	10.087(62)	9.96(17)	30.13(20)
*CTE values are multiplied by 10^{-6}			

https://doi.org/10.1180/mgm.2024.105 Published online by Cambridge University Press